CHAPTER-3

Cu(I) substituted Wurtzite ZnO: A Novel Room Temperature Lead-Free Ferroelectric and High-κ Giant Dielectric

3.1 Introduction

Semiconducting Ferroelectric materials have technological importance due to extensive applications in optoelectronic devices for uses in optical communication, memory, display, and coherent optical processing.[1-6] The specific device applications also include capacitors, modulators, beam deflectors, light valves, and holographic storage media. Further, one of the efficient ways to scavenge electrical energy through vibration-based energy harvesting is by utilization of piezoelectric and ferroelectric materials. Ferroelectric bulk crystals are desired for usage in optoelectronic devices because of the combination of extraordinary optical and electronic properties originating from their non-Centro symmetric crystal structure and structural anisotropy that exhibit many nonlinear optical properties. Using field effects coupled by high-κ dielectrics and ferroelectric polarizations, the electric properties of ferroelectric semiconductors have been widely tuned to facilitate the emergence of various gate-modulated devices such as transistors, logic inverters and memory storage devices, light-emitting diodes (LEDs) and photodetectors.

Wurtzite piezoelectric ZnO, with the highest piezoelectricity, can be the attractive choice for doping transition metal ions in host lattices to develop novel ferroelectric materials.[7-9] Zinc Oxide (ZnO) is considered one of the very important metal oxides due to its unique chemical and physical properties such as electrochemical coupling, good chemical and photostability, and wide range of radiation absorption capabilities.[10-11]Further ZnO is a very low-toxicity semiconductor that has been implemented successfully in biomedicine and pro-ecological systems.[12-13] Although pure ZnO can exhibit ferroelectricity, the polarization switching is not observed until its melting point (1975^{o}C) because of the large activation energy accompanied by the dipole switching process.

ZnO has also been considered for spintronic applications: if doped with 1–10% of magnetic ions (Cu, Mn, Fe, Co, V, etc.), ZnO could become ferromagnetic even at room temperature.[14-17] Substitution of ZnO with different elements such as Fe, Al, Ni, Cu, and Mg, can optimize the band gap of ZnO and that will give the needed flexibility for application in modern optoelectronic devices.[18-20] Cu is one of the promising dopants because of its high abundance low toxicity and multiple electronic state ($Cu^{+}/Cu^{2+/}Cu^{3+}$) formation that can have an inbuilt effect on structural phase transitions. Therefore, the study was aimed to investigate the interaction of d^{10} cations (Zn^{2+} and Cu^{+}) in tetrahedral symmetry and the role of resultant oxygen vacancy generated through the incorporation of Cu^{+} ions in host ZnO lattice on dielectric interaction/polarizations and search of a possible ferroelectric or ultra-high κ dielectric material. There is some report on Ferroelectricity in Cu-doped ZnO thin films that may arise due to the formation of surface oxygen vacancy in ZnO thin films fabricated in ultra-vacuum conditions.[21-22] However, there is no report on the appearance ferroelectric phase in bulk ZnO-based materials. Thus, it was important to synthesize Cu^{+} doped ZnO in bulk to study dielectric properties and search for the ferroelectric transition in bulk material. For the first time by employing selective precursor, Cu(I)Cl and sol-gel method, we have been able to synthesize Cu(I) doped ZnO that shows high-κ dielectric and ferroelectricity in bulk. Synthesis, characterization, and study of dielectric/ferroelectric properties of Cu(I) doped ZnO microcrystals are presented in this chapter.

3.2 Material Synthesis and Characterizations

In the synthesis process, Cu-doped ZnO; ($Zn_{1-x}Cu_xO_{1-\delta}$) ceramic samples were prepared by the modified sol-gel route in the range of x=0.02 to 0.15. In the molar ratio, (1-x):x:1.5 ZnO, CuCl, and EDTA were taken for sample preparation. The

resultant powder obtained was of green color. The schematic of the synthesis procedure is presented in Figure 3.1 (a). Pellets were made by hydraulic press at 8 tonne in a die of ~1 cm thickness and the green pellet was heated at 1050 ^{o}C for 15 h twice to obtain a dense pellet. Images of prepared Cu-substituted ZnO powder and obtained pellet were also shown in Figure 3.1(b). The density of the pellet was measured using the Archimedes method was 97% of the theoretical density.

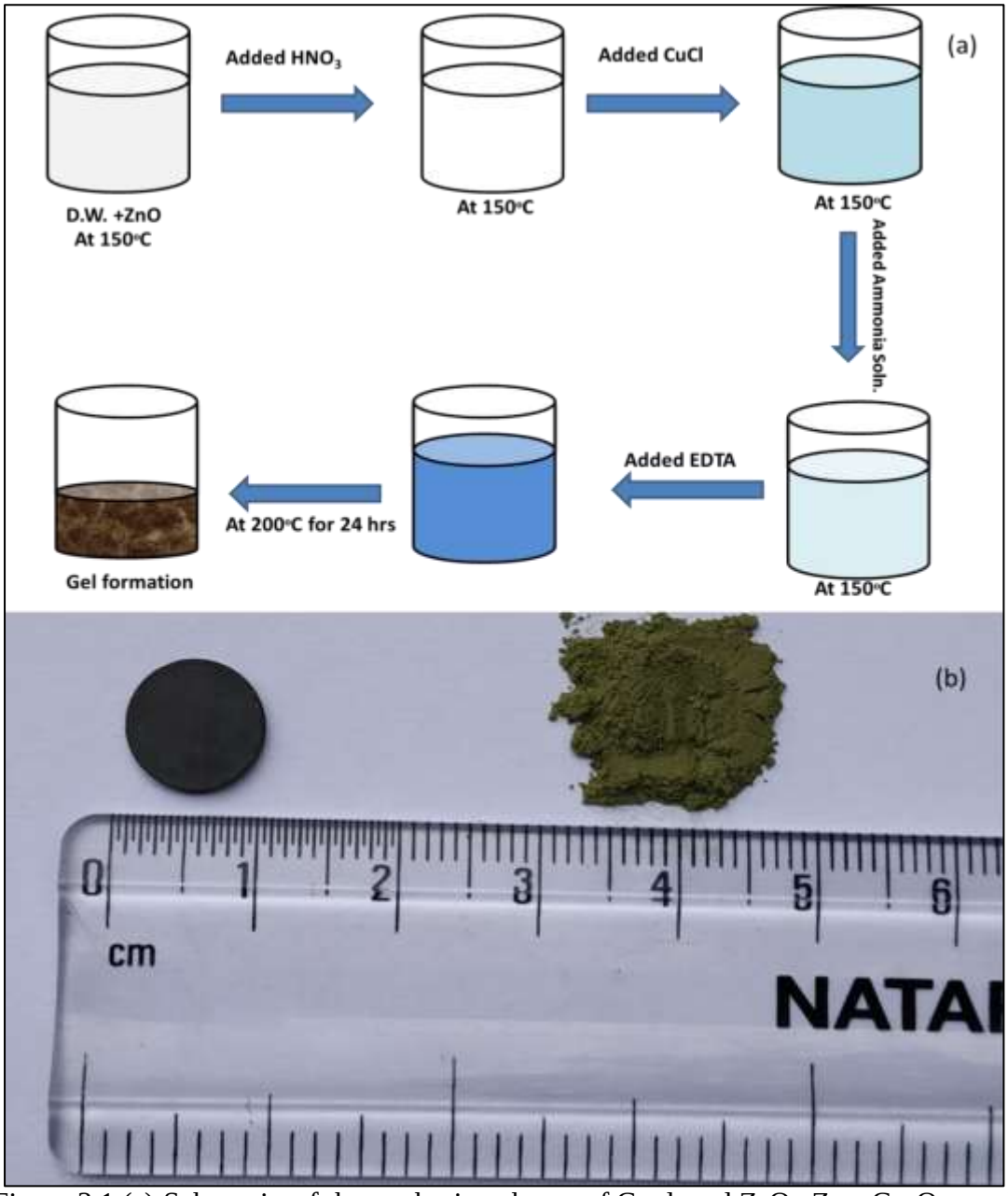

Figure 3.1 (a) Schematic of the synthesis scheme of Cu doped ZnO; $Zn_{1-x}Cu_xO_{1-\delta}$ and (b) Photograph of synthesized powder and sintered pellet of $Zn_{0.95}Cu_{0.05}O_{1-\delta}$.

The structure and phase purity of cu-doped ZnO samples were analyzed by powder x-ray diffraction (XRD) analysis. The complex impedance spectroscopic study of Cu-doped ZnO pellets was made by Metrohm Autolab (PGSTAT204) equipped with a FRA32M module. Impedance measurements were analyzed using NOVA software. For ferroelectric measurement, we have done our experiment at room temperature from 100 Hz to 500 Hz frequency range using RADIANT precision premier II. For magnetic studies of our sample $Zn_{0.95}Cu_{0.05}O_{1-\delta,}$ the fine ground powder was subjected to a Magnetic property measurement system (MPMS) by a Squid-based magnetometer (MPMS-3, Quantum Design Inc.)

3.3 Structural Study

The structural parameters and phase purity have been studied using the powder X-ray diffraction patterns.XRD patterns of $Zn_{1-x}Cu_xO_{1-\delta}$ ($x \leq 0.15$) are shown in Figure 3.2(a). Sharp and intense diffraction peaks of all the samples confirm the high crystallinity of the samples. It also reveals a clean hexagonal phase formation (sp. gp. P63mc) in Wurtzite ZnO structure for full doping range along with minute impurities of CuO phase at higher Cu doping concentrations.

Cu^+ is not stable in the air. It radially oxidizes to Cu^{2+}, which is why Cu^+ ion impurities that are not substituted in the ZnO lattice appear as CuO (Cu^{2+} oxide). Cu^+ ion is stable in the air only in the form of CuX (X= Cl, Br, and I). For the preparation of $Zn_{1-x}Cu_xO_{1-\delta}$, we heated the sample in the air that is why CuO was formed as an impurity phase.

Using FullProf software, the structure of materials was refined by the Rietveld method. The Rietveld refined XRD image of the $Zn_{0.95}Cu_{0.05}O_{1-\delta}$ phase is shown in Figure 3.2(b). The absence or negligible amount of diffraction peaks for metallic Cu,

Cu_2O, and CuO phases suggests the substitution of Cu in the ZnO lattice without altering its Wurtzite structure. The structural parameter derived from Rietveld refinement of $Zn_{1-x}Cu_xO_{1-\delta}$ ($x \leq 0.12$) is given in Table 3.1. The change in the lattice parameter of $Zn_{1-x}Cu_xO_{1-\delta}$ is almost negligible. This may be because in tetrahedral coordination, the ionic radius of Cu^+ is 0.74 Å and Cu^{2+} is0.71 Å and that is almost the same or close to the ionic radii of Zn^{2+} (0.74 Å) in tetrahedral coordination.[23] That is why, during lattice formation, Cu ions are easily able to occupy Zn sites in the Wurtzite crystal lattice. However, with the increase in the doping percentage of Cu,($x \geq 0.08$), weak diffraction peaks corresponding to the CuO phase start appearing in the powder XRD pattern (Figure 3.2 a) due to the segregation of Cu ions. Thus, only up to 8% Cu ions can be substituted on Zn^{2+} sites in the ZnO lattice.

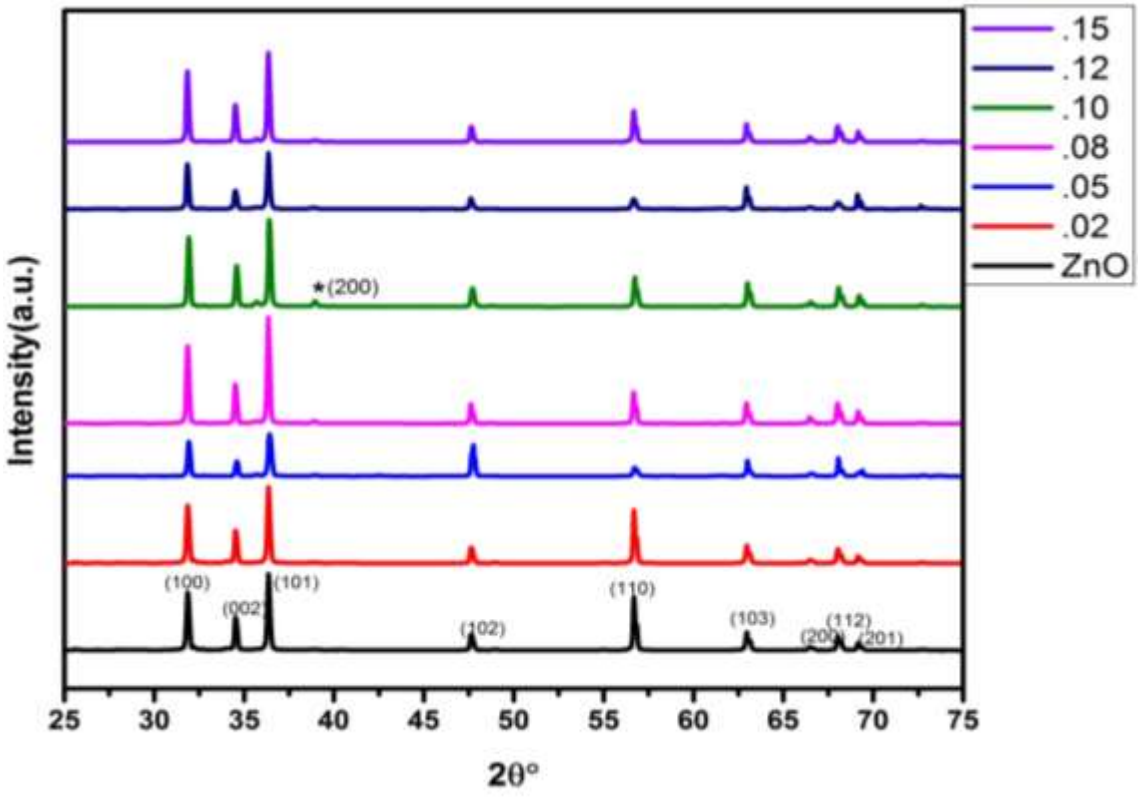

Figure 3.2 (a) Powder XRD pattern of $Zn_{1-x}Cu_xO_{1-\delta}$ ($x \leq 0.15$) samples.

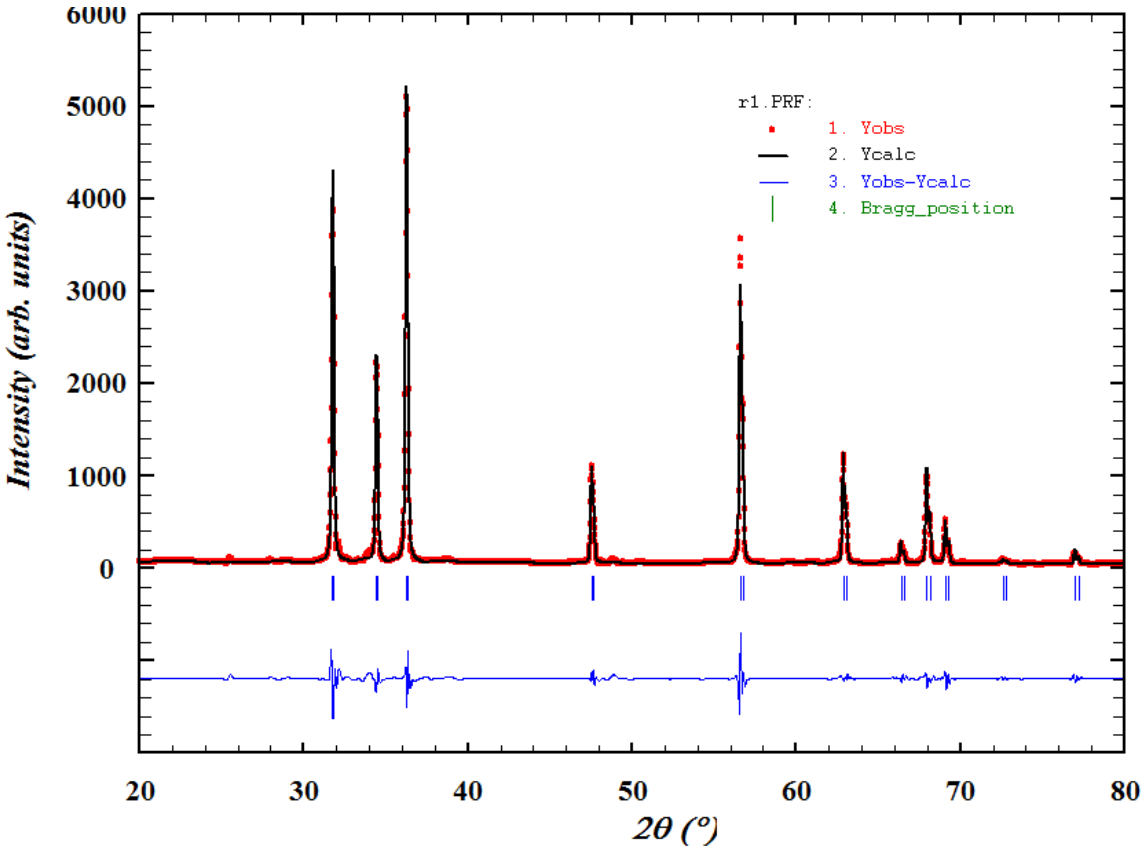

Figure 3.2(b) Rietveld refined powder XRD pattern of $Zn_{0.95}Cu_{0.05}O_{1-\delta}$

Table 3.1. Structural Parameters of $Zn_{1-x}Cu_xO_{1-\delta}$

Compound	Lattice Parameters (Å)		χ^2	R_f	R_{Bragg}	R_{wp}
	a=b	c				
$Zn_{0.98}Cu_{0.02}O_{1-\delta}$	3.249193	5.204031	1.581	6.47	7.88	14.2
$Zn_{0.95}Cu_{0.05}O_{1-\delta}$	3.251282	5.207811	2.556	7.47	6.78	15.5
$Zn_{0.92}Cu_{0.08}O_{1-\delta}$	3.251762	5.205712	2.341	6.81	7.12	15.9
$Zn_{0.9}Cu_{0.1}O_{1-\delta}$	3.251971	5.203214	2.115	7.21	6.18	16.7
$Zn_{0.88}Cu_{0.12}O_{1-\delta}$	3.252005	5.205581	2.188	6.73	7.20	17.9
$Zn_{0.85}Cu_{0.15}O_{1-\delta}$	3.251903	5.204715	3.124	7.17	6.89	17.5

3.4 SEM Study

SEM images of (a) powder and (b) intersection of the pellet of $Zn_{0.95}Cu_{0.05}O_{1-\delta}$ in Figure 3.3. The SEM study reveals that the grains are of micrometer sizes in the range of 2-50 μm and hexagonal shape. The pellets were well-sintered, and the grains were in good contact with each other. The EDX image shown in figure 3.3(c) also

confirms the composition and apparent homogeneity of the materials. EDX study has been carried out by the EDX probe attached in the SEM instrument (Figure 3.3) and indeed Zn and Cu were found in the ratio of 0.95: 0.05, which agrees well with the composition taken for the preparation. The density of the pellets was measured by the Archimedes method in water and was ~97% of the theoretical density of the material.

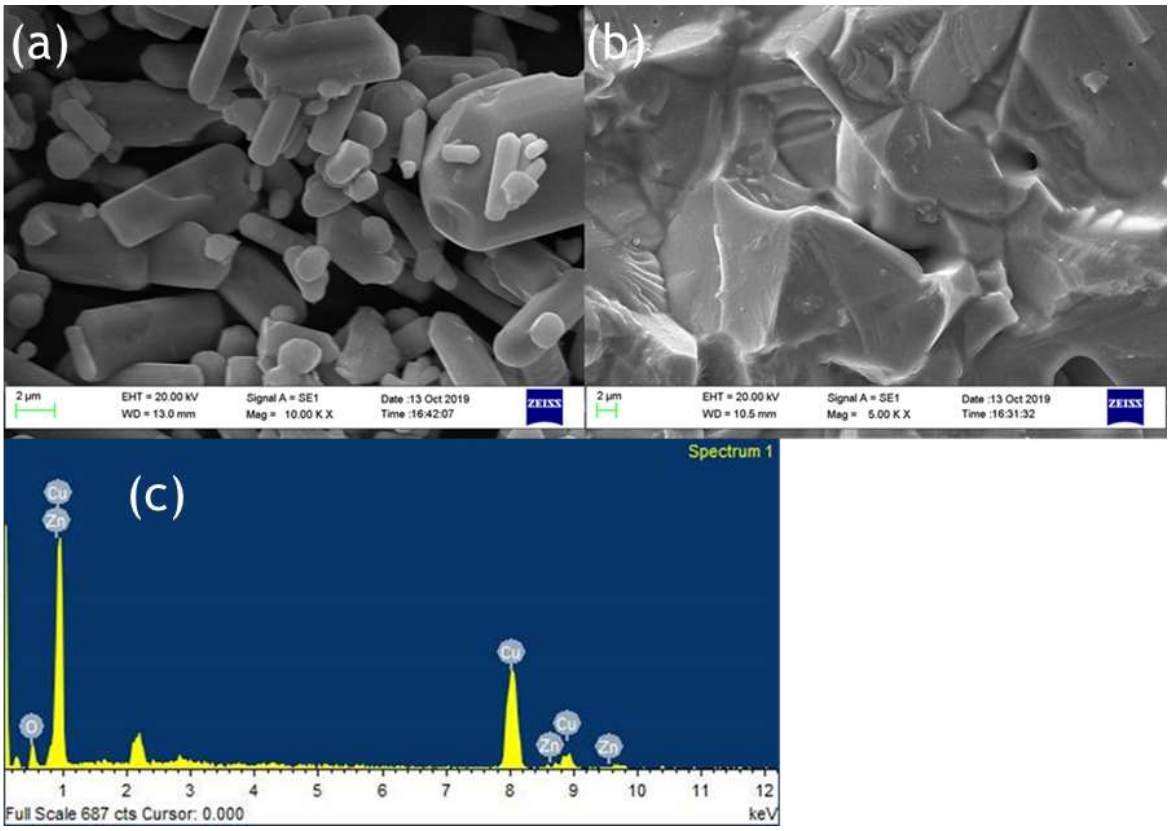

Figure 3.3 Scanning electron micrograph of $Zn0.95Cu_{0.05}O_{\delta}$ (a) powder and (b) Pellet, sintered at 1050°C for 12 h, showing clean single-phase material with distinctive grains. (c) EDX analysis shows the stoichiometric distribution of Zn, Cu, and O elements.

3.5 XPS Study

The electronic structure and oxidation states of Cu and Zn in $Zn_{0.95}Cu_{0.05}O_{1-\delta}$ samples were investigated by X-ray photoelectron spectroscopy. Core level Cu (2p) spectra of $Zn_{0.95}Cu_{0.05}O_{1-\delta}$ sample are shown in Fig. 3.4(a). The binding energy of Cu (2p3/2) is observed around 932.9eV and a very broad and weak satellite peak was observed at 10 eV from the main peak confirming that Cu ions are mostly in +1

oxidation state. In General, both Cu and Cu^{+} (2p3/2) electrons have binding energy close to 933 eV with absence or very weak presence of satellite peak.[24-25] For Cu^{2+} ions, the binding energy of 2p3/2 core electrons is 933.5 eV with the appearance of a very strong satellite peak around 940 eV.[25] Thus it is clear from the spectra of the Cu(2p) core level shown in Figure 3.4(a) that Cu exists mostly in the Cu^{+} state in $Zn_{0.95}Cu_{0.05}O_{1-\delta}$. The Zn (2p) core level spectra are shown in Figure 3.4(b). The binding energy of Zn (2p3/2) electrons was observed at 1021.5 eV. Binding Energy for 2p3/2 electrons for Zn (metal) and Zn^{2+} ions are 1021 eV and 1021.4 eV respectively.[25-26] Thus, Zn is in a 2+ oxidation state in $Zn_{0.95}Cu_{0.05}O_{1-\delta}$ samples. Therefore the presence of Cu^{+} on Zn^{2+} will generate oxygen ion vacancy $Zn_{0.95}Cu_{0.05}O_{1-\delta}$ lattice. Using Kroger vink notation, the oxygen vacancy formation is represented as

$$2Cu'_{Zn} + V_O^{\circ\circ} = \phi \qquad (3.1)$$

and the oxide-ion vacancy formation after Cu^{+} substitution on Zn^{2+} sites in the Wurtzite lattice is represented below.

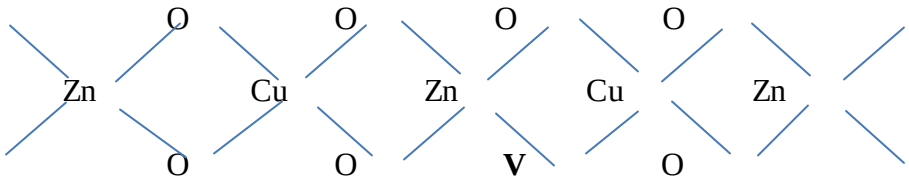

An estimate of relative concentrations of Zn and Cu was carried out from the intensities of Zn(2p) and Cu(2p) peaks in $Zn_{0.95}Cu_{0.05}O_{1-\delta}$.

Relative surface concentration is calculated from the formula:[27]

Relative concentration $C_M = (I_M / \lambda_M.\sigma_M.D_M) / \sum (I_M / \lambda_M.\sigma_M.D_M \quad)$ (3.2)

where I_M is the integrated intensity of the core levels (M= Zn(2p) and Cu(2p)), λ_M is the mean escape depth of the respective photoelectrons, σ_M is the photoionization

cross-section, and D_M is the geometric factor. The photoionization cross-section values were taken from Scofield's data[28] and mean escape depths were taken from Penn's data.[29] The geometric factor was taken as 1 because the maximum intensity in this spectrometer is obtained at 90°. Surface concentrations of Zn and Cu are found in the ratio of 0.95: 0.05 in $Zn_{0.95}Cu_{0.05}O_{1-\delta}$. Thus surface compositions of $Zn_{0.95}Cu_{0.05}O_{1-\delta}$ are almost the same as the bulk composition.

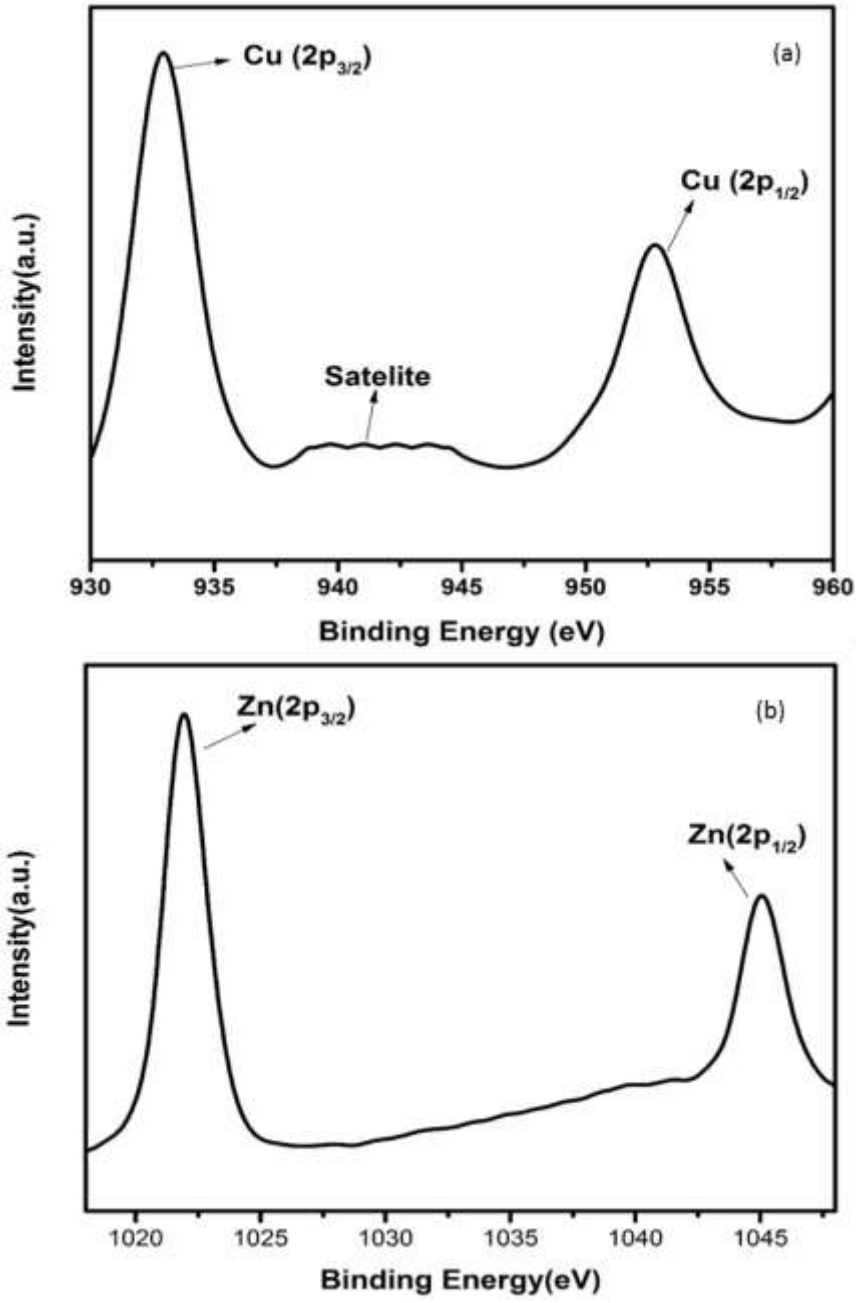

Figure 3.4 Core level XPS spectra of $Zn_{0.95}Cu_{0.05}O_{1-\delta}$. (a) Cu (2p) and (b) Zn(2p)

3.6 MPMS Study

Further to understand the electronic structure of $Zn_{0.95}Cu_{0.05}O_{1-\delta}$ samples, the magnetic response of the $Zn_{0.95}Cu_{0.05}O_{1-\delta}$ was also studied using Magnetic property measurement system (MPMS) by Squid based magnetometer (MPMS-3, Quantum Design Inc.). Figure 3.5 shows a typical magnetization vs. magnetic field (M-H) curve obtained from a $Zn_{0.95}Cu_{0.05}O_{1-\delta}$ sample at 300 K, revealing a clear diamagnetic behavior under applied magnetic fields up to ± 5 T.[30-31] Besides that, at magnetic intensities lower than ±0.2 T, the material exhibited a residual ferromagnetic signal, evident after a subtraction of the diamagnetic signal as shown in the inset of Figure 3.5.[30-31]

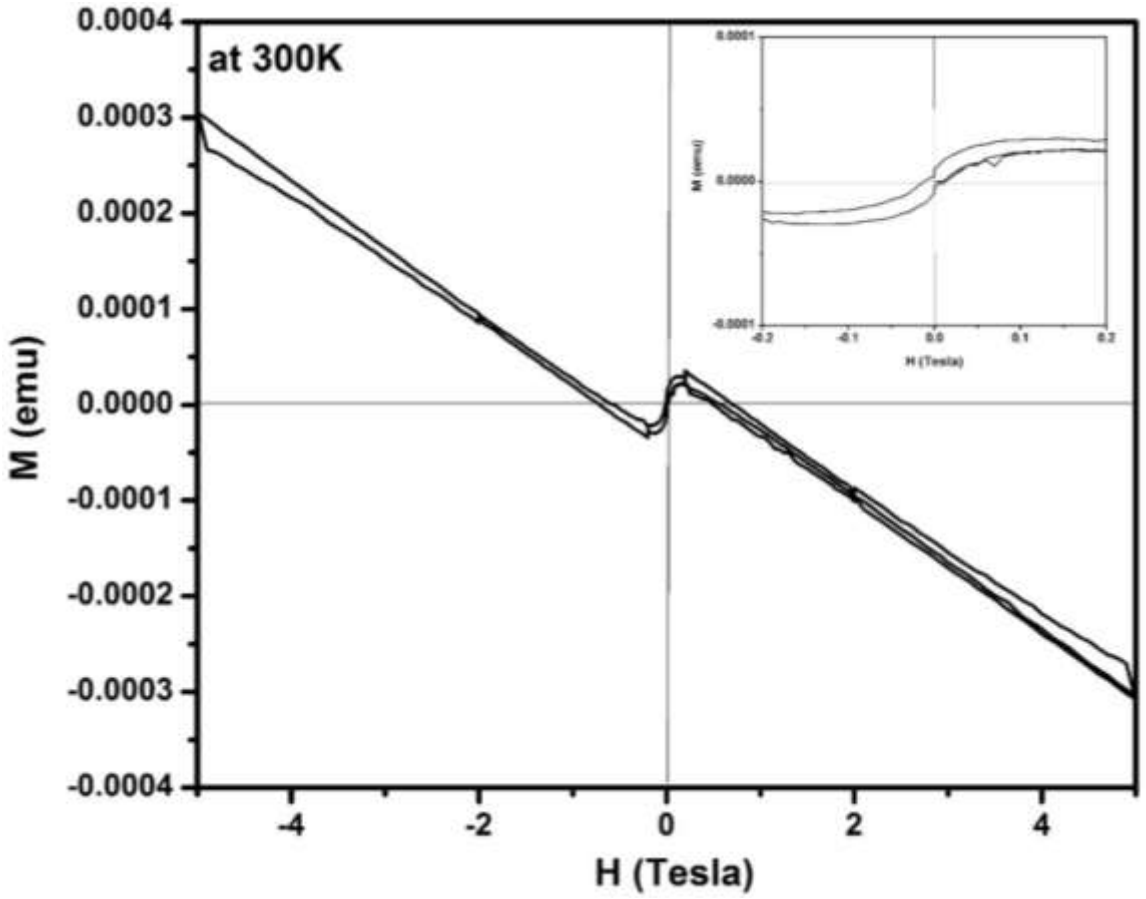

Figure 3.5 Magnetization vs. magnetic field (M-H) curve for $Zn_{0.95}Cu_{0.05}O_{1-\delta}$ sample at 300 K. Inset shows the ferromagnetic contribution within ± 0.2T.

The diamagnetic behavior of $Zn_{0.95}Cu_{0.05}O_{1-\delta}$ is largely due to presence of fully filled d orbital of Zn^{2+} and Cu^{+} having electronic configuration $3d^{10}4s^{0}4p^{0}$. The weak ferromagnetism in $Zn_{0.95}Cu_{0.05}O_{1-\delta}$ can be originated due to the polarization of unpaired 2p electrons of O with the empty 4p orbital of Zn and Cu around oxygen vacancies in Wurtzite lattice. Oxygen vacancy-induced room temperature ferromagnetisms are observed within the percolation limit in various oxide systems such as doped and un-doped ZnO, TiO_2, CeO_2, and SnO_2.[31-34] Thus the magnetization (M-H) study also confirms the oxygen vacancy formation due to the incorporation of diamagnetic Cu^{+} ion on Zn^{2+} sites in the ZnO lattice.

3.7 Dielectric Study:

The absence of oxide ion or oxygen vacancy formation can introduce net dipole moment in Zn and Cu tetrahedral and can also destabilize the local structure/coordination and distort the local polyhedral structure of Wurtzite ZnO lattice to result in ferroelectric transitions. The impedance spectroscopy was carried out at a variable temperature in the air to study the dielectric behavior of the material in the frequency range of 100 KHz to 1Hz. The dielectric constant was calculated using the formula:

$$\varepsilon_r = \frac{C*d}{\varepsilon_\circ * A} \tag{3.3}$$

Where; $\varepsilon_r$is the dielectric constant, C is capacitance, ε_o is the permittivity of free space $(8.85*10^{-12})$F/m, d is the thickness of the pellet, A is the area of the pellet;

Capacitance (C) was calculated by using the formula

$$C = -\frac{1}{\omega}\left[\frac{Z''}{Z'^2 + Z''^2}\right] \tag{3.4}$$

and the dielectric loss was calculated by

$$\tan \delta = \frac{\varepsilon''}{\varepsilon'} = \frac{Z'}{-Z''} \quad (3.5)$$

Figure 3.6(a), shows the plots of the real part of the dielectric constant (ε_r') at 100 KHz frequency (f) for the $Zn_{1-x}Cu_xO_{1-X/2}$ (x = 0.02, 0.05, 0.08, 0.1, 12 and 0.15) pellets in the temperature range of 100-650^oC. In general, the ε_r' values were increasing in the range of 100°C to 650°C with a maxima appearing around 600^oC. The maxima for the dielectric constant (ε_r') of $Zn_{1-x}Cu_xO_{1-\delta}$ appeared for x =0.05 and x=0.12. The dielectric constant (ε_r') for x=0.05 was ~6300 and for x=0.12 was ~3275 respectively at 100 kHz f at 600 ^oC. The variation in dielectric loss (tan $\delta = \varepsilon_r''/\varepsilon_r'$) with temperature, at selected frequency, is shown in Figure 3.6(b). Tanδ was ~13 for x=0.05 and ~30 for x=0.12 at 100 kHz frequency at 600 ^oC. Considering the high dielectric constant of the materials, the observed dielectric loss is quite less for $Zn_{1-x}Cu_xO_{1-\delta}$ samples. As can be seen from Figure 3.6(a), the dielectric constant of Cu doped ZnO varies with the doping of Cu, and the highest dielectric constant (6300 at 600 ^oC) at 100 kHz frequency was obtained for $Zn_{0.95}Cu_{0.05}O_{1-\delta,}$ the later studies were centralized around the dielectric and ferroelectric properties of $Zn_{0.95}Cu_{0.05}O_{1-\delta}$. Figure 3.7(a, b) show the dielectric constant and dielectric loss for $Zn_{0.95}Cu_{0.05}O_{1-\delta}$ samples at various temperature in the range of 100-650 ^oC at variable frequencies. It was found that both dielectric constant and dielectric loss were increasing continuously up to 600 ^oC at all frequencies. However, both dielectric constant and dielectric loss were decreased with increasing frequencies. The increase in dielectric constant (ε_r') with increasing temperatures at different frequencies for $Zn_{1-x}Cu_xO_{1-\delta}$ is likely due to the localized nature of hopping charge carriers in addition to interfacial polarization due to space charge. These extrinsic contributions to ε_r' are expected to contribute

significantly only at higher frequencies. Further, it was also observed that the maximum dielectric constant and maximum dielectric loss were obtained at T_m= 600^{o}C between the frequency range of 10 kHz to 100 kHz.

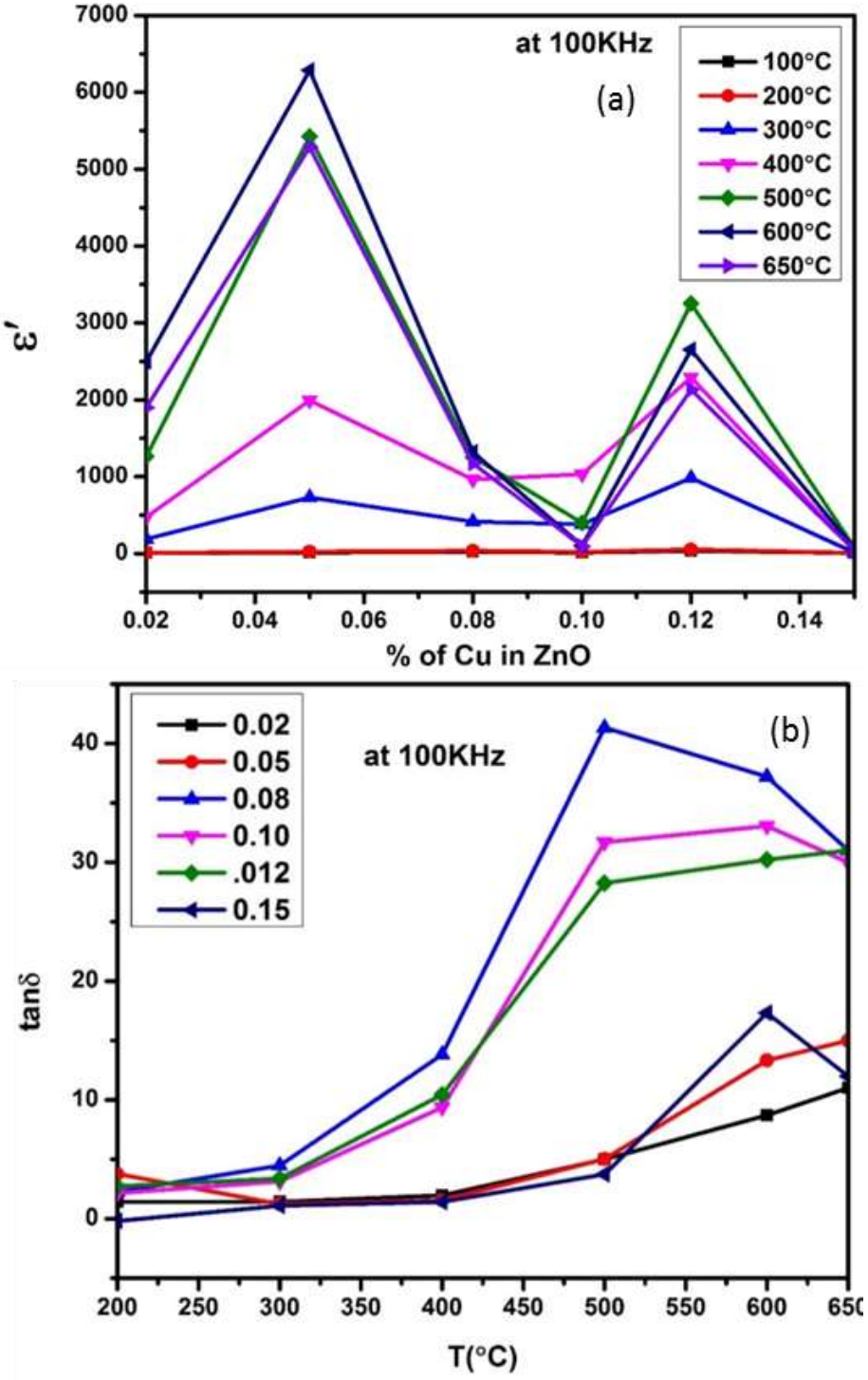

Figure 3.6 (a) Variation of dielectric constant and (b) Variation of dielectric loss for Cu+ ion substitution in ZnO lattice at 100 KHz with the increase in temperature.

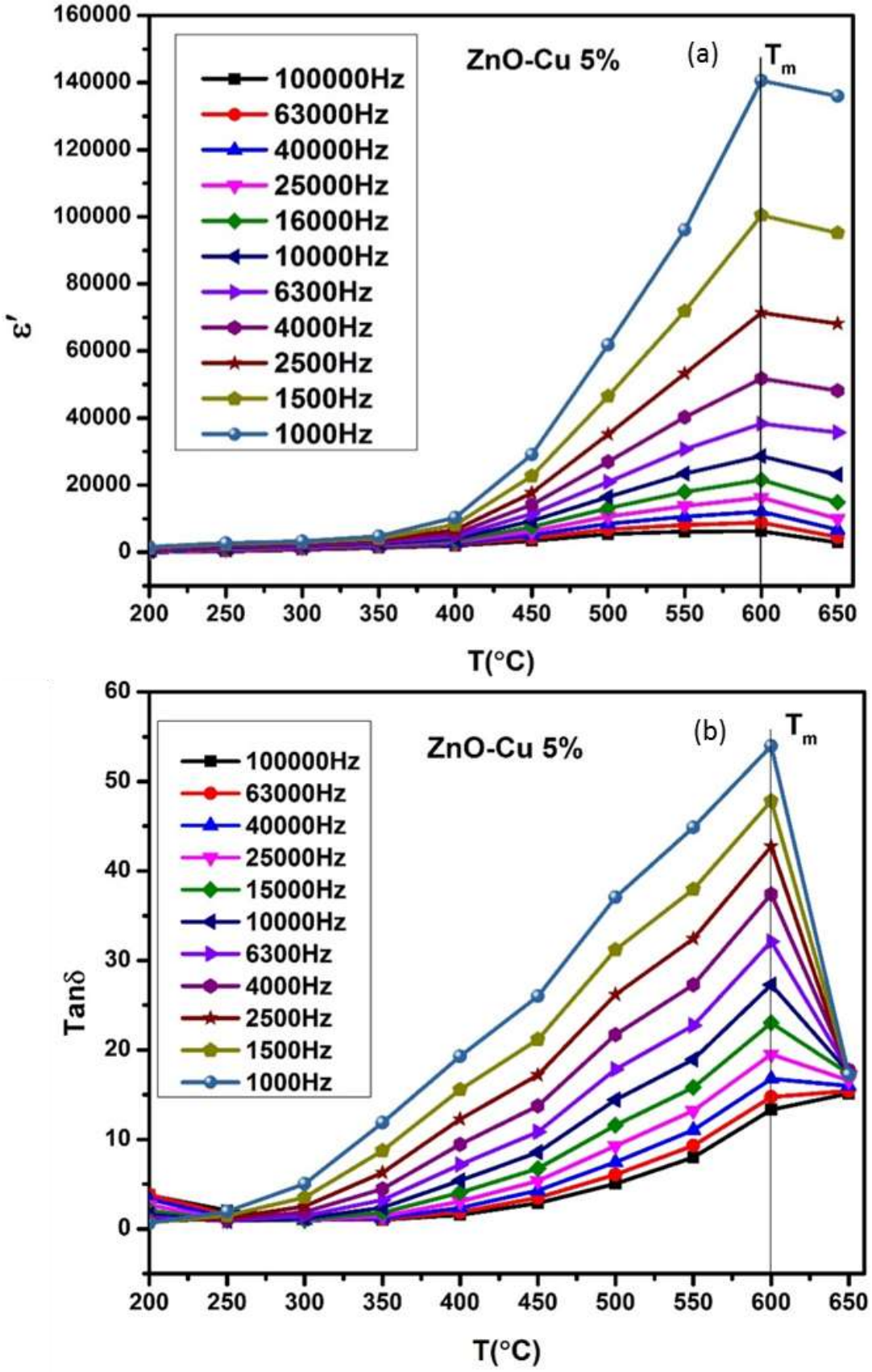

Figure 3.7 (a) Variation of dielectric constant and (b) Variation of dielectric loss of $Zn_{0.95}Cu_{0.05}O_{1-\delta}$ pellets at various frequencies with the increase in temperature.

3.8 Ferroelectric Study

This suggests that the behavior of the material is not relaxor type as Tm does not vary with applied frequencies. Therefore P-E characteristic of the material was studied at room temperature using RADIANT precision Premier II. The measured polarization hysteresis loop for Cu-doped ZnO; $Zn_{0.95}Cu_{0.05}O_{1-\delta}$ is shown in Figure 3.8. The observation of the clear hysteresis-loop behavior, by a Sawyer-Tower circuit, with the external applied field confirms the existence of ferroelectricity in bulk $Zn_{0.95}Cu_{0.05}O_{1-\delta}$ pellets at room temperature. In our knowledge, this is the first report of the formation of a clear P-E hysteresis-loop for any bulk ZnO-based samples. The values of remnant polarization Pr and Vc were found $9.60*10^{-03}$ ($\mu C/cm^2$) and $3.83*10^{+02}$(V/cm), respectively, for $Zn_{0.95}Cu_{0.05}O_{1-\delta}$. The values of Pr and Vc are quite low, however, the formation of P-E hysteresis-loop in Cu^+ doped ZnO samples opens a new direction in making binary nontoxic ferroelectrics and understanding the role oxygen vacancy and transition metal ion d orbital interaction with oxygen 2p orbital in binary oxides.

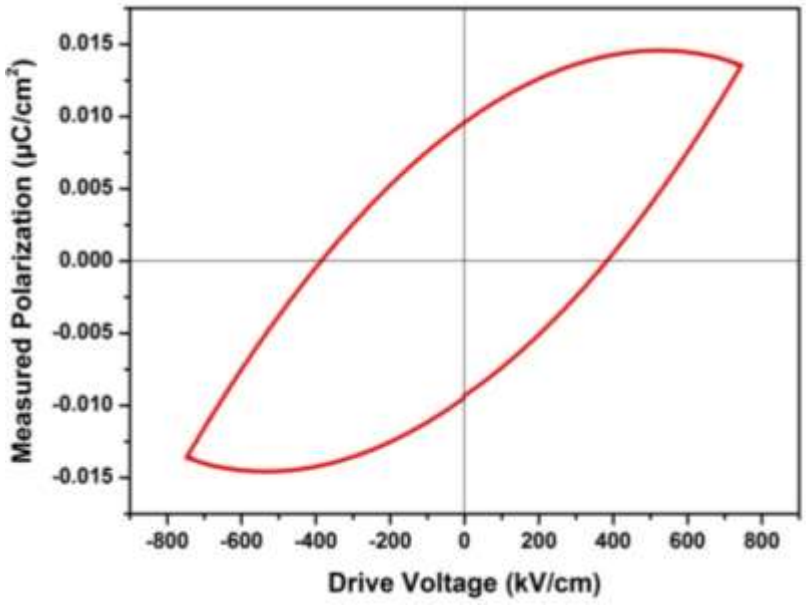

Figure 3.8 Plot of polarization (P) Vs. Electric field (E) for $Zn_{0.95}Cu_{0.05}O_{1-\delta}$ pellets at room temperature.

The materials $Zn_{0.95}Cu_{0.05}O_{1-\delta}$ also exhibit ferroelectricity at room temperature with remnant polarization Pr and Vc equal to $9.60*10^{-03}$ μC/cm^2 and $3.83*10^{+02}$V/cm respectively. However, the other materials of Cu and Zn systems from thin film have relatively higher values for ferroelectricity, the values of the ZnO: Cu (8 at.%) were investigated. As the frequency increases, the maximum polarization decreases from ≈ 0.78 μ C cm − 2 at 500 Hz to ≈ 0.72 μ C cm − 2 at 2 kHz. The shape of the P–E loops and the remnant polarization were found to exhibit little frequency dependence in the range of 0.5 to 2 kHz. [21] However, this is the first report of ferroelectricity in the bulk samples. We believe that if our samples can be fabricated in the form of thin film, with highly aligned grain, high remnant polarization can be achieved.

3.9 CONCLUSIONS

The quest to develop or identify ferroelectric in binary oxide materials led us to envisage oxygen vacant structure in strong insipient dielectric hosts such as Wurtzite ZnO lattice. Cu^+ ion substitution on Zn^{2+} sites not only resulted in net polarization but also opened the path for strong polarization between O-2p and filled d^{10} Zn/Cu 4p orbital in tetrahedral coordination. Cu^+ ion substitution on Zn^{2+} sites in ZnO lattice is achieved by careful selection of raw material CuCl and adaptation of low-temperature sol-gel synthesis route for the preparation of bulk material. Up to 8% of Cu^+ ions were substituted in the ZnO lattice and the highest dielectric constant (~6300) was obtained at 600^{o}C for $Zn_{0.95}Cu_{0.05}O_{1-\delta}$ at 100 KHz frequency. The materials $Zn_{0.95}Cu_{0.05}O_{1-\delta}$ also exhibit ferroelectricity at room temperature with remnant polarization Pr and Vc equal to $9.60*10^{-03}$ μC/cm^2 and $3.83*10^{+02}$ V/cm respectively.

References:

1. Optical Response of High-Dielectric-Constant Perovskite-Related Oxide, C. C. Homes, T. Vogt, S. M. Shapiro, S. Wakimoto, A. P. Ramirez, Science 2001, 293, 673−676.
2. Nanowire electronic and optoelectronic devices, Y. Li, F. Qian, J. Xiang, and C. M. Lieber, Materials Today, 2006, 9(10) 18-27.
3. Above-band gap voltages from ferroelectric photovoltaic devices, S. Y. Yang, J. Seidel, S. J. Byrnes, P. Shafer, C.-H. Yang, M. D. Rossell, P. Yu, Y.-H. Chu, J. F. Scott, J. W. Ager III, L. W. Martin & R. Ramesh, Nature Nanotechnology 2010, 5, 143–147.
4. Ferroelectric field effect enhanced electro resistance in metal/ferroelectric/semiconductor tunnel junctions, Z. Wen, C. Li, D. Wu, A. Li, N. Ming, Nature Materials, 2013, 12, 617–621.
5. Semiconducting ferroelectric photovoltaics through Zn^{2+} doping into $KNbO_3$ and polarization rotation, F. Wang, I. Grinberg, and A. M. Rappe, Phys. Rev. B, 2014, 89, 235105(1-5)
6. A lead-halide perovskite molecular ferroelectric semiconductor, W-Q. Liao, Y. Zhang, C. Hu, J-G. Mao, H-Y. Ye, P. Li, S. D. Huang & R. Xiong, Nature Commun., 2015 (6) 7338 (1-7)
7. Piezoelectric Nano Generators Based on Zinc Oxide Nanowire Arrays, Z. L.Wang and J. Song, Science, 2006, 312(5771), 242-246.
8. Mechanically Powered Transparent Flexible Charge- Generating Nanodevices with Piezoelectric ZnO Nanorods, M. Choi, D. Choi, M. Jin, I. Kim, S. Kim, J. Choi, S. Y. Lee, J. M. Kim and S. W. Kim, Adv. Mater.2009,21,2185–2189.
9. Piezoelectric Field Effect Transistor and Nanoforce Sensor Based on a Single ZnO Nanowire, X. Wang, J. Zhou, J. Song, J. Liu, N. Xu, and Z. L. Wang, Nano Lett., 2006, 6 (12), 2768-2772.
10. The effects of zinc nitrate, zinc acetate, and zinc chloride precursors on investigation of structural and optical properties of ZnO thin films, E. Bacaksiz, M. Parlak, M. Tomakin, A. Ozcelik, M. Karakız, M. Altunbas, Journal of Alloys and Compounds, 2008, 466, 447–450.
11. Analysis of Optical Absorbance Spectra for the Determination of ZnO Nanoparticle Size Distribution, Solubility, and Surface Energy, D. Segets, J.

Gradl, R. Klupp Taylor, V. Vassilev, and W. Peukert, ACS Nano, 2009, 3(7), 1703-1710.

12. Electrical conduction and dielectric studies of ZnO pellets, M. Chaari and A. Matoussi, Physica B 407 (2012) 3441–3447.
13. A strategy for ZnO nanorod mediated multi-mode cancer treatment, H. Zhang, B. Chen, H. Jiang, C. Wang, H. Wang, X. Wang, Biomaterials, 2011, 32, 1906-1914.
14. Search for ferromagnetism in transition-metal-doped piezoelectric ZnO, N. A. Spaldin, Phy. Rev. B, 2004, 69, 125201 (1-7).
15. Anisotropic Ferromagnetism in Substituted Zinc Oxide, M. Venkatesan, C. B. Fitzgerald, J. G. Lunney, and J. M. D. Coey, Phys. Rev. Lett. 2004, 93, 177206(1-4).
16. Chemical Manipulation of High-TC Ferromagnetism in ZnO Diluted Magnetic Semiconductors, K. R. Kittilstved, N. S. Norberg, and D. R. Gamelin, Phys. Rev. Lett., 2005, 94, 147209 (1-4).
17. Room-temperature ferromagnetism in Cu doped ZnO thin films, D. B. Buchholz, R. P. H. Chang, J.-Y. Song, and J. B. Ketterson, Appl. Phys. Lett., 2005, 87, 082504 (1-3)
18. ZnO nanostructures for optoelectronics: Material properties and device applications, A. B. Djurisic´, A. M. C. Ng, X. Y. Chen, Progress in Quantum Electronics, 2010, 34, 191–259.
19. Synthesis and optical properties of Ni-doped zinc oxide nanoparticles for optoelectronic applications, R. Elilarassi and G. Chandrasekaran, Optoelectronics Letters, 2010, 6(1), 6–10.
20. The optoelectronic properties and role of Cu concentration on the structural and electrical properties of Cu doped ZnO nanoparticles, K. Omri, A. Bettaibi, K. Khirouni, L. El Mir, Physica B: Condensed Matter, 2018, 537, 167–175.
21. Mutual Ferromagnetic–Ferroelectric Coupling in Multiferroic Copper-Doped ZnO, T. S. Herng, M. F. Wong, D. Qi, J. Yi, A. Kumar, A. Huang , F. C. Kartawidjaja , S. Smadici , P. Abbamonte , C. Sánchez-Hanke , S. Shannigrahi , J. M. Xue , J. Wang , Y. P. Feng , A. Rusydi , * K. Zeng,* and J. Ding, Adv. Mater. 2011, 23, 1635–1640.

22. Ferroelectric liquid crystal matrix dispersed with Cu doped ZnO nanoparticles, D. P. Singh, S. K. Gupta, K. K. Pandey, S. P. Yadav, M. C. Varia and R. Manohar, Journal of Non-Crystalline Solids, 2013, 363, 178–186.
23. Revised Effective Ionic Radii and Systematic Studies of Interatomic Distances in Halides and Chalcogenides, R.D. Shannon, Acta Cryst. 1976, A32 751-767.
24. Advanced analysis of copper X-ray photoelectron spectra, Mark C. Biesinger, Surf. Interface Anal. 2017, 49, 1325–1334.
25. Resolving surface chemical states in XPS analysis of first-row transition metals, oxides, and hydroxides: Sc, Ti, V, Cu and Zn, Mark C. Biesinger, Leo W.M. Laua, Andrea R. Gerson, Roger St. C. Smart, App. Surf. Sc., 2010, 257, 887–898.
26. XPS primary excitation spectra of Zn2p, Fe2p, and Ce3d from ZnO, α-Fe_2O_3, and CeO_2, N. Pauly, F. Yubero, J. P. Espinós and S. Tougaard, Surf. Interface. Anal.2019, 51, 353–360.
27. C. J. Powell and P. E. Larson, Appl. Surf. Sci., 1978, 1, 186–201.
28. J. H. Scofield, J. Electron Spectrosc. Relat. Phenom., 1976, 8, 129–137.
29. D. R. Penn, J. Electron Spectrosc. Relat. Phenom., 1976, 9, 29–40.
30. Influence of Ga vacancies, Mn and O impurities on the ferromagnetic properties of GaN micro- and nanostructures, G. Guzmán, R Escudero, R Silva and M. Herrera, Journal of Applied Physics, 2018, 123, 161578 (1-9).
31. Effects of structural, optical, and ferromagnetic states on the photocatalytic activities of Sn–TiO_2 nanocrystals,A.S.Ganeshraja, S.Thirumurugan,K. Rajkumar, K.Zhu,Y.Wang, K.Anbalagan and J.Wang, RSC Adv.,2016,6,409–421
32. Oxygen vacancy induced ferromagnetism in Cu-doped ZnO, M. Zhu, Z. Zhang, M. Zhong, M. Tariq, Y. Li, W. Li, H. Jin, K. Skotnicova and Y. Li, Ceramics International,2017, 43, 3166–3170.
33. Oxygen Vacancy Induced Room Temperature Ferromagnetism in Pr-Doped CeO_2 Thin Films on Silicon, G. Niu, E. Hildebrandt, M. A. Schubert, F. Boscherini, M. H. Zoellner, L. Alff, D. Walczyk, P.Zaumseil, I. Costina, H. Wilkens and T. Schroeder, ACS Appl. Mater. Interfaces 2014, 6, 20, 17496-17505.
34. Oxygen-vacancy-induced ferromagnetism in undoped SnO2 thin films, G. S. Chang, J. Forrest, E. Z. Kurmaev, A. N. Morozovska, M. D. Glinchuk, J. A. McLeod, A. Moewes, T. P. Surkova, and Nguyen Hoa Hong, Phy. Rev. B, 2012, 85, 165319 (1-9).